GLACE: The Global Land-Atmosphere Coupling Experiment.

2. Analysis

Zhichang Guo[1], Paul A. Dirmeyer[1], Randal D. Koster[2], Gordon Bonan[3], Edmond Chan[4], Peter Cox[5], C.T. Gordon[6], Shinjiro Kanae[7], Eva Kowalczyk[8], David Lawrence[9], Ping Liu[10], Cheng-Hsuan Lu[11], Sergey Malyshev[12], Bryant McAvaney[13], J.L. McGregor[6], Ken Mitchell[11], David Mocko[10], Taikan Oki[14], Keith W. Oleson[3], Andrew Pitman[15], Y.C. Sud[2], Christopher M. Taylor[16], Diana Verseghy[4], Ratko Vasic[17], Yongkang Xue[17], and Tomohito Yamada[14]

4 February 2005

[1] Center for Ocean-Land-Atmosphere Studies, Calverton, MD, 20705, USA
[2] NASA Goddard Space Flight Center, Greenbelt, MD, 20771, USA
[3] National Center for Atmospheric Research, Boulder, CO 80307, USA
[4] Meteorological Service of Canada, Toronto, Ontario M3H 5T4, Canada
[5] Hadley Center for Climate Prediction and Research, Exeter EX1 3PB, UK
[6] Geophysical Fluid Dynamics Laboratory, Princeton, NJ 08542, USA
[7] Research Institute for Humanity and Nature, Kyoto 602-0878, Japan
[8] CSIRO Atmospheric Research, Aspendale, Victoria 3195, Australia
[9] University of Reading, Reading, Berkshire RG66 BB, UK
[10] Science Applications International Corporation, Beltsville, MD 20705, USA
[11] National Center for Environmental Prediction, Camps Springs, MD 20746, USA
[12] Princeton University, Princeton, NJ 08544, USA
[13] Bureau of Meteorology Research Centre, Melbourne, Victoria 3001, Australia
[14] University of Tokyo, Tokyo 153-8505, Japan
[15] Macquarie University, North Ryde, New South Wales 2109, Australia
[16] Centre for Ecology and Hydrology, Wallingford, Oxfordshire OX10 8BB, UK
[17] University of California, Los Angeles, CA 90095, USA

Submitted to J. Hydrometeorology on February 11, 2005

Abstract

The twelve weather and climate models participating in the Global Land-Atmosphere Coupling Experiment (GLACE) show both a wide variation in the strength of land-atmosphere coupling and some intriguing commonalities. In this paper, we address the causes of variations in coupling strength – both the geographic variations within a given model and the model-to-model differences. The ability of soil moisture to affect precipitation is examined in two stages, namely, the ability of the soil moisture to affect evaporation, and the ability of evaporation to affect precipitation. Most of the differences between the models and within a given model are found to be associated with the first stage – an evaporation rate that varies strongly and consistently with soil moisture tends to lead to a higher coupling strength. The first stage differences reflect identifiable differences in model parameterization and model climate. Intermodel differences in the evaporation-precipitation connection, however, also play a key role.

1. Introduction

Interaction between the land and atmosphere plays an important role in the evolution of weather and the generation of precipitation. Soil moisture may be the most important state variable in this regard. Much research has been conducted on the effects of soil wetness variability on weather and climate, encompassing various observational studies (e.g., Namais 1960; Betts et al. 1996; Findell and Eltahir 2003) and theoretical treatments (e.g., Entekhabi et al 1992, Eltahir 1998). These studies notwithstanding, the strength of land-atmosphere interaction is tremendously difficult to measure and evaluate. Consider, for example, attempts to quantify the impact of soil moisture on precipitation through joint observations of both. Precipitation may be larger when soil moisture is larger, but this may tell us nothing, for the other direction of causality – the wetting of the soil by precipitation – almost certainly dominates the observed correlation. Global-scale or even regional-scale estimates of land-atmosphere coupling strength simply do not exist.

This difficulty motivates the use of numerical climate models to address the land-atmosphere feedback question. With such models, idealized experiments can be crafted and sensitivities carefully examined. A few recent examples include the studies of Dirmeyer (2001), Koster and Suarez (2001), Schlosser and Milly (2002), and Douville (2003).

Modeling studies, of course, are far from perfect. The ability of land states to affect atmospheric states in atmospheric general circulation models (AGCMs) is not explicitly prescribed or parameterized, but is rather a net result of complex interactions between numerous process parameterizations in the model. As a result, land-atmosphere interaction varies from model to model, and this model dependence affects AGCM-based interpretations of land use

impacts on climate, soil moisture impacts on precipitation predictability, and so forth (Koster et al. 2002). The broad usage of GCMs for such research and the need for an appropriate interpretation of model results makes necessary a comprehensive evaluation of land-atmosphere interaction across a broad range of models. The Global Land-Atmosphere Coupling Experiment (GLACE) was designed with this in mind.

In GLACE, twelve AGCMs perform the same highly-controlled numerical experiment, an experiment designed to characterize quantitatively the general features of land-atmosphere interaction. In GLACE, three 16-member ensembles of 3-month simulations are performed: an ensemble in which the land states of the different members vary independently (W); an ensemble in which the same geographically- and temporally-varying land states are prescribed for each member (R), and an ensemble in which only the subsurface soil moisture values are prescribed for each member (S). By quantifying the inter-ensemble similarity of precipitation time series within each ensemble and then comparing this similarity between ensembles, we can isolate the impact of the land surface on precipitation – we can quantify the degree to which the atmosphere responds consistently to anomalies in land states (hereafter referred to as the "land-atmosphere coupling strength"). The companion paper (Koster et al., this issue) describes the experiment and analysis approach in detail and provides an overview of the model comparison.

Note that the focus on subsurface moisture (ensemble S above) is of special interest. It is well accepted that the variability of soil moisture is much slower than that of atmospheric states (Dirmeyer 1995). Hope for improving the accuracy of seasonal forecasts lies partly with the "memory" provided by soil moisture. By quantifying the impact of subsurface soil moisture on

precipitation, GLACE helps evaluate a model's ability to make use of this memory in seasonal forecasts.

Koster et al. (this issue) and Koster et al. (2004) highlight "hot spots" of land-atmosphere coupling -- regions of strong coupling between soil moisture and precipitation that are common to many of the AGCMs. What causes such commonalities, and how do they relate to climatological and hydrological regime? Which aspects of land surface and atmospheric parameterization cause the large model-to-model differences of coupling strength among the AGCMs? How are the signals that exist in the land surface states transmitted to and manifested in the atmosphere states?

Such critical questions, which arise naturally from a survey of the GLACE results and lie at the heart of our understanding of land-atmosphere feedback, are addressed in the present paper. First, section 2 addresses the geographical patterns of coupling strength seen in the models. Section 3 then provides an analysis of intermodel differences in coupling strength. Further discussion and a summary of our findings are presented in section 4.

2. Commonalities in coupling strength

The multi-model synthesis used in the companion paper (Koster et al., this issue) proves to be an effective way to identify robust (across models) regions of significant soil moisture impact on precipitation and near-surface air temperature – the commonalities in geographic pattern synthesized from the approach are less subject to the quirks or deficiencies of any individual model. We can apply the same multi-model analysis procedure here to the other model variables. As in the companion paper (see section 5 of Part 1), we first disaggregate

variables from each model to the same fine grid, one with a resolution of $0.5^o \cdot 0.5^o$. We average the results computed on that grid with equal weights.

As explained in the companion paper, the variable Ω_v measures the degree to which the sixteen time series for the variable v generated by the different ensemble members are similar, or coherent. Thus, $\Omega_v(S)$- $\Omega_v(W)$ or $\Omega_v(R)$- $\Omega_v(W)$ are measures of the control of land states on the atmospheric variable v. As in the companion paper, we computed Ω_v and the standard deviation σ_v for each model across 224 aggregated 6-day totals (16 ensemble members times 14 intervals in each simulation time-series).

The upper left panel of Fig. 1 shows the mean of $\Omega_P(S) - \Omega_P(W)$ for precipitation across the 12 models, i.e., the model-average impact of subsurface soil moisture on precipitation. This figure essentially repeats the contents of the top panel of Figure 10 from the companion paper. Notice that the larger soil moisture impacts on precipitation generally occur in the transition zones between humid and arid climates, such as the central Great Plains of North America, the Sahel in Africa, and the northern and western margins of the Asian monsoon regions.

How can we characterize the evaporation signal that best serves as a link between soil moisture anomalies and precipitation – that best explains the geographical variations of $\Omega_P(S)$ - $\Omega_P(W)$ shown in the figure? In Figure 2, we argue that such an evaporation signal (as a proxy for the full surface energy balance) must have two characteristics: it must respond coherently to soil moisture variations, and it must show wide temporal variations. The four panels show idealized evaporation time-series for 16 parallel ensemble members under four situations: (i) a low coherence in the evaporation time series [i.e., a low value of $\Omega_E(S) - \Omega_E(W)$] and a low

variability of evaporation [i.e., a low value of $\sigma_E(W)$]., (ii) a low coherence but a high variability of evaporation, (iii) a high coherence yet a low variability of evaporation, and (iv) a high coherence and a high variability of evaporation. Clearly, cases (i) and (ii) cannot lead to a robust precipitation response (across ensemble members) to soil moisture, given that evaporation is the key link between the two, and evaporation itself has no coherent response to soil moisture. A coherent evaporation response, however, does not by itself guarantee a coherent precipitation response. For case (iii), the evaporation response to soil moisture is robust, but the atmosphere would not see a strong signal at the surface due to the low evaporation variability. Only the fourth situation provides a signal for the atmosphere that is both coherent and strong.

We argue that for soil moisture to affect evaporation, both $\Omega_E(S) - \Omega_E(W)$ and $\sigma_E(W)$ must be suitably high. In other words, the product $(\Omega_E(S) - \Omega_E(W)) \cdot \sigma_E(W)$ must be high. We use this diagnostic product throughout this paper to characterize the ability of the evaporation signal to support land-atmosphere feedback. (We assume here that $\sigma_E(W)$ and $\sigma_E(S)$ are similar; analysis of the model data confirms this.) The product proves effective for our purposes, despite being a potentially suboptimal diagnostic – it may, for example, already contain some implicit feedback information through the potential co-evolution of σ_E and σ_P, and thus it may reflect in part the character of the atmosphere and its role in feedback. Still, the other direction of causality (precipitation variability causing evaporation variability) is undoubtedly dominant, and regardless of the source of the evaporation variability, the product still serves as a characterization of the evaporation signal itself.

The upper right panel of Fig. 1 shows the global distribution of $\Omega_E(S)$- $\Omega_E(W)$ (again, averaged across the models), and the lower left panel shows that for $\sigma_E(W)$. Neither diagnostic by itself explains all characteristics of the distribution of $\Omega_P(S) - \Omega_P(W)$ (top left panel) . The lower right panel shows the distribution of the product $(\Omega_E(S)- \Omega_E(W)) \cdot \sigma_E(W)$ averaged over the 12 models. The spatial correlation between the geographical patterns of $\Omega_P(S) - \Omega_P(W)$ and the product is 0.42, which is larger than that between $\Omega_P(S) - \Omega_P(W)$ and either factor alone (0.36 and 0.2 for $\sigma_E(W)$ and $\Omega_E(S) - \Omega_E(W)$, respectively).

Note that none of these spatial correlations is particularly large. The diagnostic product $(\Omega_E(S)- \Omega_E(W)) \cdot \sigma_E(W)$, however, will be shown to prove very effective in characterizing intermodel differences in coupling strength at a given location, much better than can either factor alone (see section 3). The overall performance of the diagnostic product suggests that the coupling between precipitation and soil moisture is largely local and confirms that the coupling is strongest in regions having both a coherent evapotranspiration (ET) signal and a high ET variability.

The scatter plots in Figure 3 illustrate further the control of hydrological regime on the product $(\Omega_E(S)- \Omega_E(W)) \cdot \sigma_E(W)$. The lines represent a best fit through the mean of the dependent variable in bins of 200 points each. A roughly linear inverse relationship is seen between the soil wetness and $\Omega_E(S)- \Omega_E(W)$. The scatter plot shows that ET is more sensitive to land state in dry climates than in areas with moderate soil wetness. The results are consistent with the findings of Dirmeyer et al. (2000), who showed that the sensitivity of surface fluxes to variations in soil moisture generally concentrates at the dry end of the range of soil moisture

index. In contrast, the standard deviation of ET (σ_E) is not large for low soil moisture, simply because of the small values of ET in such regions. Put together, the product $(\Omega_E(S)-\Omega_E(W)) \cdot \sigma_E(W)$ has minima for very wet and very dry soils, and it is largest for intermediate soil moisture values (degree of saturation between 0.1 and 0.4; see Figure 3c). Figure 3d shows, for comparison, how $\Omega_P(S)-\Omega_P(W)$ varies with soil moisture; the relationship shows a hint of that seen for $(\Omega_E(S)-\Omega_E(W)) \cdot \sigma_E(W)$, particularly at the extremes.

A study of Figure 3 thus suggests the following interpretation. In wet climates, ET is controlled not by soil moisture but by atmospheric demand (as determined in part by net radiation) since soil moisture is plentiful there, and specifying surface land states in the numerical experiments has little impact there on ET and rainfall generation (cases i and ii in Figure 2). In dry climates, ET rates are sensitive to soil moisture, but the typical variations are generally too small to affect rainfall generation (case iii in Figure 2). Only in the transition zone between wet and dry climates, where ET variations are suitably high but are still sensitive to soil moisture, do the land states tend to have strong impacts on precipitation.

The conclusions above were obtained from a multi-model average. We now examine, with some simple statistical indicators, their relevance to individual models. First, consider the panels on the left in Fig. 4. The top panels show the inter-model standard deviation of $\Omega(S)-\Omega(W)$ among the 12 models, and the bottom panels show the ratio of the mean to the standard deviation. The pattern of the inter-model standard deviation of $\Omega_E(S)-\Omega_E(W)$ (left) largely resembles the field of $\Omega_E(S)-\Omega_E(W)$ itself (Fig. 1), except for enhanced variability over arid regions. The ratio serves as a measure of signal to noise, showing where there is the least uncertainty among models. The pattern of the ratio resembles that of the mean in the upper right

panel in Fig. 1, with some shift away from the arid regions, giving a distribution that overlaps many of the world's major agricultural areas.

The implication of the left panels in Fig. 4 is that the regions of strong ET coherence are relatively robust among the models, and not an artifact of extreme values in a small number of models. The same cannot be said about precipitation coherence (Ω_P(S)- Ω_P(W)). The right panels in Fig. 4 show the standard deviation and signal-to-noise ratio for precipitation coherence. The ratio of the mean to the standard deviation for precipitation coherence is much weaker than for ET and more dominated by noise. Only over a few regions (e.g., northern India, China, Pakistan, and parts of sub-Saharan Africa) are there sizeable areas that approach a ratio of unity (note the difference in scale). Note also that the strongest signal-to-noise values are still located in regions with strong levels of 12-model mean precipitation coherence in the upper left panel of Fig. 1. Large, inter-model variability, however, predominates over most of the globe.

3. Comparison among GCMs

While the models show some similarities in the geographical pattern of land-atmosphere coupling strength, they also show some wide disparities. Global maps of Ω_P(S)- Ω_P(W) were provided in Fig. 5 of Part 1 for all twelve GCMs. The major features found in the multi-model mean are seen in many of the models. Some areas, though, such as the Northern Amazon and Orinoco Basins, show significant differences. Also, the coupling strength in general seems relatively large in the GFDL, NSIPP, and CAM3 models, whereas that for GFS/OSU seems very weak. Some models even show negative values in places, suggesting an increase of noise when land conditions are synchronized among ensemble members. This may be the result of sampling

error or unrealistic vertical gradients, and thus fluxes, induced when land surface variables are specified without regard for the atmospheric conditions (e.g. Reale et al. 2002).

Similar commonalities and disparities among AGCMs can be found in the impacts of soil moisture on ET. We showed in section 2 that the diagnostic $(\Omega_E(S)- \Omega_E(W)) \cdot \sigma_E(W)$, which measures the degree to which the evaporation signal is both coherent and strong, explains much of the geographical variation in precipitation coherence for the mean of the models. Figure 5 shows global maps of this product for each model. The models tend to agree in the placement of larger values in the transition regions between humid and dry climates. As for disparities, the GFDL model has the highest mean values for the product, whereas GFS/OSU has by far the lowest. Indeed, the low values for GFS/OSU by themselves can explain this model's globally low precipitation coherence values.

The diagnostic largely explains, at a given region, the intermodel differences in the land-atmosphere coupling strength. Figure 6 shows how $(\Omega_E(S)-\Omega_E(W)) \cdot \sigma_E(W)$ varies with $\Omega_P(S)- \Omega_P(W)$ for the average of global ice-free land points and for the three "hot spot" regions delineated by dashed lines in Fig. 1. The intermodel differences in $(\Omega_E(S)-\Omega_E(W)) \cdot \sigma_E(W)$ clearly explain much of the intermodel differences in $\Omega_P(S)-\Omega_P(W)$. Indeed, the square of the correlation coefficient between the two quantities are 0.77, 0.82 and 0.60 over the Sahel, northern India, and the central Great Plains of North America, respectively. (Supplemental calculations show $\Omega_E(S)- \Omega_E(W)$ alone would produce an r^2 of 0.84, 0.56, and 0.38, respectively, while $\sigma_E(W)$ alone would produce an r^2 of 0.20, 0.61, and 0.40, respectively.)

Of course, the relationship is not perfect, due to sampling error, to the inability of the diagnostic to capture fully the evaporation signal's impact on land-atmosphere feedback, and to the fact that the models also differ in the coupling mechanism between ET and precipitation (section 3.3). Indeed, the separation of the pathway linking soil moisture anomalies and precipitation generation into two parts – the segment between soil moisture anomalies and evaporation anomalies and that between evaporation anomalies and precipitation generation – is useful for understanding the intermodel differences in $\Omega_P(S)$- $\Omega_P(W)$. In essence, Figure 6 suggests that while the first segment is the most important for explaining these differences, it is not all-important.

In the remainder of this section, we focus on the models' representations of these two segments. We construct a series of indices to measure the overall strength of each segment within each model, as well as the strength of coupling for the entire path from soil wetness to precipitation. The results are summarized in Table 1.

3.1 *Soil-precipitation coupling: Net effect*

The first two columns after the list of models in Table 1 show the global mean of the precipitation coherence $\Omega_P(S)$- $\Omega_P(W)$ calculated over all non-ice land points. The next column provides the rank of the model (1 indicating the highest index, and thus the model with the strongest control of sub-surface soil moisture on precipitation). The models are sorted by their overall score in this index. Some grouping is evident; three models (GFDL, NSIPP and CAM3) show similarly high values of this index (between 0.032 and 0.040), and another group (CSIRO, UCLA, CCSR, COLA, GEOS, and BMRC) shows much lower values, ranging from 0.006-0.014.

The HadAM3 and GFS/OSU models show almost no impact of sub-surface soil wetness on precipitation. The HadAM3 result is consistent with findings from a recent study (Lawrence and Slingo 2004) that showed how the inclusion of predicted vegetation phenology in this model had no impact on precipitation, even though soil wetness, surface latent heat flux, and near surface air temperature were all significantly affected over large areas of the globe.

A comparison of the R and S experiments reveals how the specification of "faster" land variables (temperatures, etc.) affects the model rankings. In Fig. 7, global means of Ω_P(S)-Ω_P(W) are plotted against Ω_P(R)- Ω_P(W) for each model. Similar groupings are evident. Notice that the rankings are similar, despite the differences in the scales of the axes. In general, if specifying subsurface soil moisture has a relatively large impact on the coherence of rainfall in a model, then the specification of all land variables in the model will also have relatively large impact on precipitation.

3.2 *Segment 1: Soil-ET coupling*

Again, the first segment of the path in soil-precipitation coupling is from soil wetness variations to ET variations, which we characterize with the diagnostic $(\Omega_E(S)- \Omega_E(W)) \cdot \sigma\sigma_E(W)$. Columns 4 and 5 in Table 1 show respectively the global mean of this diagnostic for each model (calculated over all non-ice land points) and the rank of the model based on the diagnostic. The GFDL model clearly has the strongest link between subsurface soil wetness and ET. There is a significant gap to the model in second place (CCCma) and then a fairly continuous spectrum in the diagnostic down to the 11th model (COLA). GFS/OSU has a very weak coupling between

soil wetness and ET and is a clear outlier. Note that the centers of the topmost soil layers of the GFDL, BMRC, CCCma and HadAM3 models are deeper than 5 cm, meaning that for each of these four models, the soil moisture was continually specified in the topmost layer in the S experiment. Thus, for these four models, bare soil evaporation was directly affected by the soil moisture specification.

As discussed in section 2, the diagnostic $(\Omega_E(S)- \Omega_E(W)) \cdot \sigma_E(W)$ captures two separate aspects of the evaporation signal: its variability and its coherence. Figure 8 shows, using bin curves, how these two components of the diagnostic tend to depend on soil moisture. The variability of evaporation appears to be largest for intermediate soil wetness values, and the range in coherence is largest for low and intermediate values. As should be expected, the bin curves differ between the models. For most values of soil wetness, the GFDL model has the largest coherence of ET, and GFS/OSU has the smallest coherence. GFDL also shows the largest variability for evaporation. The stratification of the curves in the bottom panel agrees well with the rankings of SW? ET in Table 1.

Figure 9 shows, for each of the regions analyzed in Figure 6, the individual quantities σ_E and $\Omega_E(S)- \Omega_E(W)$ for each model. This breakdown helps us relate differences in the soil-ET coupling to differences in climate regime and model parameterization. We speculate, in fact, that differences in σ_E relate mostly to differences in the models' background climatologies (though σ_E may potentially be amplified through its coevolution with σ_P during feedback) and that differences in $\Omega_E(S)- \Omega_E(W)$ relate mostly to differences in incident radiative energy and in the details of the land surface parameterization – particularly, in those details defining the

sensitivity of evaporation to soil moisture variations. For example, notice that globally BMRC tends to have moderately high coherence in its evaporation fluxes ($\Omega_E(S)$- $\Omega_E(W)$) but very low variability (σ_E) – the type of behavior idealized in the third panel of Figure 2. The low σ_E for BMRC presumably reflects the relatively low mean and variability of the precipitation forcing (not shown) for that model over most of the areas examined – i.e., it results from the model's background climatology. The same arguments regarding evaporation variability apply, to a degree, to the CCSR/NIES model, particularly over northern India and the Sahel. The GFDL model, on the other hand, shows relatively high precipitation variability on a global scale, helping to promote evaporation variability. Coupled with the moderate-to-high $\Omega_E(S)$- $\Omega_E(W)$ values for this model, the diagnostic ($\Omega_E(S)$- $\Omega_E(W)$) $\cdot$ $\sigma_E(W)$ is especially high, promoting strong land-atmosphere feedback.

Now consider the COLA model. Evaporation (and precipitation) variability in the areas studied is not particularly small for this model, but the evaporation coherence values are (case ii in Fig 2). These low coherence values probably reflect in large part this model's relatively high inter-ensemble variability of net radiation (not shown).

Again, details of the land model parameterization – particularly those associated with soil-water limited transpiration – presumably explain most of the intermodel differences in $\Omega_E(S)$- $\Omega_E(W)$. The parameterization in the GFS/OSU model, for example, must be responsible for this model's very low $\Omega_E(S)$- $\Omega_E(W)$. (Curiously, though, a later version of the OSU land model – the NOAH LSM – shows substantial evaporation sensitivity to soil moisture variations when coupled to NCEP's Eta regional model [Berbery et al., 2003].) A proper analysis of such

model parameterization differences would necessarily be complex and will not be addressed in this paper.

Other climatic factors may also lead to intermodel differences in $(\Omega_E(S)- \Omega_E(W)) \cdot \sigma_E(W)$. For example, because this diagnostic peaks at intermediate values of soil wetness (Figures 3 and 8), the model whose climatology produces the highest fractional area with such soil wetness values might produce the highest average value for the diagnostic. Also, if a model shows large coherence in evaporation rates in the free-running W experiment ($\Omega_E(W)$) due to the initialization procedure or due to the effects of the oceanic boundary conditions and seasonal radiation forcing applied, the difference $\Omega_E(S)- \Omega_E(W)$ may have a small upper potential limit. Careful analysis of the model output, however, shows that neither factor has a first-order impact on the ranking of the models.

Finally, a comparison of the evaporation diagnostics computed from the R and S experiments provides some interesting insights into the control of evaporation in the different models. Fig. 10a shows the global mean (over non-ice land points) of $(\Omega_E(S)- \Omega_E(W)) \cdot \sigma_E(W)$ versus the corresponding global mean of $(\Omega_E(R)- \Omega_E(W)) \cdot \sigma_E(W)$. Because more variables (i.e., the fast variables, including surface soil moisture, skin temperature and canopy interception) are specified in the R experiment than in the S experiment, we expect the evaporation coherence to be larger for the R experiment, and thus we expect $(\Omega_E(R)- \Omega_E(W)) \cdot \sigma_E(W)$ to be larger than $(\Omega_E(S)- \Omega_E(W)) \cdot \sigma_E(W)$. This is seen in general on the global scale. Some models (CAM3, GFS/OSU, and COLA) show a relatively large difference between $(\Omega_E(R)- \Omega_E(W)) \cdot \sigma_E(W)$ and $(\Omega_E(S)- \Omega_E(W)) \cdot \sigma_E(W)$, suggesting that evaporation in these models is more strongly controlled

by the fast variables. The higher values of the diagnostic for the R experiment have consequent impacts on the land-atmosphere coupling strength in that experiment, $\Omega_P(R)$- $\Omega_P(W)$ (Figure 7).

Similar behavior is observed over the Great Plains and the Sahel (Fig. 10bd). Interestingly, the specification of the fast variables over India (Fig. 10c) apparently has an impact on only a handful of models (COLA, UCLA, GFS/OSU, CAM3, and CCCma) – the rest of the models fall close to the 1:1 line.

3.3 *Segment 2: ET-precipitation coupling*

The land surface model and the background climatology may combine to produce a strong and coherent evaporation signal, as in the lowest panel of Figure 2, but for this to be translated into an impact on precipitation, the second segment of land-atmosphere feedback – the link between evaporation and precipitation – must be strong. Returning to Table 1, we present two different indices to measure this link. Both indices are inferred from joint analysis of precipitation and ET coherences.

The first index is simply the spatial pattern correlation between $(\Omega_E(R)- \Omega_E(W)) \cdot \sigma_E(W)$ and $\Omega_P(R)- \Omega_P(W)$ across the globe. The idea is simple: if the control of ET on precipitation is local and strong, then the spatial patterns of the evaporation diagnostic and the precipitation coherence should be highly correlated. The correlations from the R experiment are similar to those from the S experiment; we use those from the R experiment here simply because they will not be spuriously high due to the response of bare soil evaporation or interception loss to incident precipitation.

The second index is the ratio between the global means (over non-ice land points) of $\Omega_P(S) - \Omega_P(W)$ and $(\Omega_E(S) - \Omega_E(W)) \cdot \sigma_E(W)$. This gives a global measure of how the second segment of land-atmosphere coupling, that is between evaporation and precipitation, degrades the link between soil moisture and precipitation, without regard for the "localness" or "remoteness" of the evaporation impacts.

Table 1 shows that the two indices produce similar rankings among the models in most cases. The CAM3 and NSIPP models rank considerably higher than the other models in both indices, suggesting that their parameterizations for moist convection, boundary layer physics, and/or other atmospheric processes are especially sensitive to evaporation variations at the land surface. GEOS and HadAM3 show much lower rankings for the ET? Precip. index than for the SW? ET index, suggesting that the ET-precipitation connection is weak enough to lose whatever signal is transmitted from soil wetness to ET. Both CAM3 and COLA show strong values of the ET-Precip. indices but do not rank high in the SW? ET index, suggesting that these models might have an even stronger coupling between soil wetness and precipitation if a different land surface parameterization were used or (in the case of the COLA model) if the net radiation was less variable. Finally, the small values of all indices for GFS/OSU and BMRC suggest that the lack of signal in ET may prevent any measure of ET? Precip coupling; again, a change of land surface scheme might alter dramatically the behavior of these two models.

The ratio-based index $(ET? Precip)_2$ can be used to interpret the scatter plot in the upper left panel in Fig. 6. That plot shows the relationship between globally-averaged numerator $\Omega_P(S) - \Omega_P(W)$ and denominator $(\Omega_E(S) - \Omega_E(W)) \cdot \sigma_E(W)$ for the different models; the fact that the r^2 value for the plot is about 0.45 implies that the SW? ET segment of land-atmosphere coupling is responsible for about half of the intermodel variations in coupling strength on the

global scale. (Again, in the individual hotspot regions, the SW? ET segment is responsible for much more.) The relationship in the top left panel of Figure 6 is not perfect. The CAM3 and NSIPP models lie well above a fitted line through the points. The interpretation of the ratio-based index (ET? Precip)$_2$ explains why: these two models have atmospheres that are (relatively) sensitive to evaporation variations. Similarly, the fact that GEOS and HadAM3 lie below the fitted line can be explained by the relative insensitivity of their atmospheres to evaporation variations.

Figure 11 summarizes the results of separating land-atmosphere feedback into the two segments. The x-axis represents the first segment of the coupling, the link between soil wetness and ET. The y-axis represents the second segment, the link between ET and precipitation as provided by the correlation-based diagnostic (ET? Precip)$_1$. The number near each model name in Fig. 11 shows how the model ranks in total coupling strength over all ice-free land points (from Table 1).

The coupling strength in a model, of course, is controlled by the nature of both segments of the coupling. The closer a model is to the upper right corner of the plot, the more likely a soil wetness anomaly can propagate through the ascending branch of the hydrologic cycle and affect precipitation. The figure immediately highlights some of the results outlined above; for example, the low coupling strengths of the BMRC and COLA models results from their weak soil moisture - evaporation connection, whereas the high coupling strength for the GFDL model results from its very strong soil moisture - evaporation connection. Coupling strength in the NSIPP and CAM3 models is strong mostly because of the strong connection between ET and precipitation in these two models. The HadAM3, on the other hand, shows the weakest coupling

between ET and precipitation, and it thus has one of the weakest coupling strengths. The GFS/OSU model lies near the origin and has the weakest coupling strength because both soil moisture - evaporation connection and coupling between ET and precipitation are weak.

3.4 *Link between differences in the coupling strength and AGCM parameterizations.*

Coupling strength is a net result of complex interactions between numerous process parameterizations in the AGCM. We have discerned different behaviors of land-atmosphere coupling among the 12 GCMs in this study and have broken down the contributions to this coupling from the atmospheric and terrestrial branches of the hydrologic cycle. Can we identify the process parameterizations that are mostly responsible for the differing coupling strengths? We now examine subsurface soil wetness and moist convective precipitation with this in mind.

The surface component of land variability cannot be a source of useful long-term memory in the climate system. However, comparison of its role to that of subsurface soil wetness in the coherence of ET is a useful metric for discriminating among the various model behaviors. Examination of the patterns of the ratio $(\Omega_E(S) - \Omega_E(W))/(\Omega_E(R) - \Omega_E(W))$ in Fig. 12 shows that the ET of the GFS/OSU, COLA, and CAM3 models is dominated by surface state variable controls (surface soil moisture, skin temperature and canopy interception), consistent to what we found in Fig. 10. Regions for which the models have ET rates less than 1 mm d^{-1} are masked in the figure, since such low ET rates can produce spurious ratios. The models in the main cluster are distinguished by their strong subsurface soil moisture impacts in semi-arid and semi-humid regions, but generally not in the deep tropics and other humid zones. CSIRO shows a pattern that is somewhat reversed, with high values of the ratio over the many humid regions,

and low values over grasslands and agricultural regions. Overall, these results suggest that certain ET parameterization frameworks – frameworks defined by imposed vegetation maps, fractional vegetation coverage, vertical structure of soil layers, and so on – might favor the coupling between sub-surface soil moisture and surface moisture fluxes (e.g., through transpiration), while others might favor surface evaporation. Note that it is not the mean ET rate, but the variability, particularly the covariability between soil wetness, ET and ultimately precipitation, that determines the strength of the coupling.

Given that moist convective precipitation is often instigated by variations in near surface air temperature and humidity, whereas large scale condensation is strongly controlled by variations in the general circulation, we might naturally expect moist convection to be a key component of the pathway linking soil moisture variations and precipitation. Figure 13 shows the global average of $\Omega_P(S)$- $\Omega_P(W)$ calculated separately from total precipitation, from convective precipitation, and from large-scale precipitation. (Note that only five models reported the precipitation components separately.) The fact that $\Omega_P(S)$- $\Omega_P(W)$ tends to be larger for convective precipitation than for large-scale precipitation supports the idea that convective precipitation is more amenable than large-scale condensation to land surface moisture variations. In the bottom panel of Fig. 13, the $\Omega_P(S)$- $\Omega_P(W)$ values are weighted by the fractional contributions of the convective precipitation component to total precipitation. This plot shows that convective precipitation bears most of the signal of soil moisture's impact on precipitation, due in large part to the dominance of convective precipitation during boreal summer. Based on the bottom plot, the coupling between surface fluxes and precipitation is indeed via the convective precipitation scheme in the AGCMs.

4. Summary

Through coordinated numerical experiments with a dozen AGCMs as part of the GLACE project, the impacts of soil moisture conditions on rainfall generation have been examined for the boreal summer season. These impacts are found to be a function of hydroclimatological regime and are heavily affected by the complex physical process parameterizations implemented in the AGCM.

In general, impacts of soil moisture on rainfall are strong only in the transition zones between dry and wet areas. Multi-model analysis shows that the existence of "hot spots" of land-atmosphere coupling in these areas is due to the coexistence of a high sensitivity of ET to soil moisture and a high temporal variability of the ET signal. In wet areas, ET is insensitive to soil moisture variations, and in dry areas, the ET variability is too weak.

The impact of soil moisture on rainfall varies widely from model to model. The GFDL, CAM3, and NSIPP models have the strongest land-atmosphere coupling strengths, and GFS/OSU, HadAM3, BMRC, and GEOS have the weakest (Table 1). The breakdown of the coupling mechanism into two segments, the link between soil moisture and evaporation and the link between evaporation and precipitation, helps to identify some of the reasons for these differences. Some models (CAM3, NSIPP) have a high coupling strength because their modeled atmospheres are strongly sensitive to evaporation variations, whereas the atmospheres of other models (HadAM3, GEOS) are relatively insensitive to evaporation variations, leading to a weak coupling strength. Most of the intermodel differences in coupling strength, however, can be explained by intermodel differences in the nature of the evaporation signal itself, as characterized by the diagnostic product $(\Omega_E(S)- \Omega_E(W)) \cdot \sigma_E(W)$. Figure 6 suggests that in the hotspot regions

of strong coupling, intermodel variations in the diagnostic product can explain about 80% of intermodel variations in coupling strength. Figures 9a and 11 summarize the impacts of the various factors on globally-averaged coupling strength for each model.

The fact that convective precipitation bears most of the signal of soil moisture's impact on precipitation suggests that the coupling between surface fluxes and precipitation is indeed mostly via convective precipitation in the AGCMs. Examination of the relative controls of subsurface soil wetness and the faster surface variables on ET coherence shows that certain ET formulations favor the coupling between sub-surface soil moisture and surface moisture fluxes, while others do not. Further analysis of intermodel variations in vegetation coverage, root zone depth, and so on may be instructive in this regard.

Indeed, for the understanding of land-atmosphere coupling strength, we can identify several broader issues that require further attention. First, an objective quantification of coupling strength from observational data needs to be obtained; its absence is a major obstacle to the evaluation of model performance. Second, land-atmosphere coupling strength should be quantified for other seasons; presumably it will be weaker during seasons that feature less moist convection, though preliminary experiments with the CCSR/NIES model (not shown) suggest otherwise. Third, for a more detailed analysis of coupling strength in a more controlled setting, different configurations of convective precipitation schemes, boundary layer schemes, and ET formulations should be applied within individual models.

Acknowledgments

GLACE is a joint project of the Global Energy and Water Cycle Experiment (GEWEX) Global Land Atmosphere System Study (GLASS) and the Climate Variability Experiment (CLIVAR) Working Group on Seasonal-Interannual Prediction (WGSIP), all under the auspices of the

World Climate Research Programme (WCRP). Computational support for the model runs was provided by the authors' institutions and associated funding agencies. Coordination of the results was supported by National Aeronautics and Space Administration grant NAG5-11579.

References

Berbery, E.H., Y. Luo, K. E. Mitchell, and A. K. Betts, 2003: Eta model estimated land surface processes and the hydrologic cycle of the Mississippi basin. *J. Geophys. Res.*, **108**, 8852, doi:10.1029/2002JD003192.

Betts, A.K., J.H. Ball, A.C.M. Beljaars, M.J. Miller and P. Viterbo, 1996: The land surface-atmosphere interaction: A review based on observational and global modeling perspectives. *J. Geophys. Res.*, **101**, 7209-7225.

Dirmeyer, P.A., 1995: Meeting on problems in initializing soil wetness. *Bull. Amer. Meteor. Soc.*, **76**, 2234-2240.

Dirmeyer, P.A., 2001: An evaluation of the strength of land-atmosphere coupling. *J. Hydrometeor.*, **2**, 329-344.

Douville, H., 2003: Assessing the Influence of Soil Moisture on Seasonal Climate Variability with AGCMs. *J. Hydrometeor.*, **4**, 1044–1066.

Eltahir, E. A. B., 1998. A Soil Moisture- Rainfall Feedback Mechanism, 1. Theory and Observations, *Water Resources Research*, **34**, 765-776.

Entekhabi, D., I. Rodriguez-Iturbe, and R.L. Bras, 1992: Variability in large-scale water balance with land surface-atmosphere interaction. *J. Climate*, **5**, 798-813.

Findell, Kirsten L. and Elfatih A.B. Eltahir, 2003: Atmospheric Controls on Soil Moisture-Boundary Layer Interactions; Part II: Feedbacks Within the Continental United States. The J. *Hydrometeor.*, **4**, 570-583.

Hollinger, S.E., and S.A. Isard, 1994: A soil moisture climatology of Illinois. *J. Climate*, **7**, 822-833.

Koster, R.D., and M.J. Suarez, 2001: Soil moisture memory in climate models. *J. Hydrometeor.*, **2**, 558-570.

Koster, R.D., P.A. Dirmeyer, A.N. Hahmann, R. Ijpelaar, L. Tyahla, P. Cox, and M.J. Suarez, 2002: Comparing the Degree of Land-Atmosphere Interaction in Four Atmospheric General Circulation Models. *J. Hydrometeor*., **3**, 363-375.

Koster, R.D., P.A. Dirmeyer, Z.-C. Guo, G. Bonan, E. Chan, P. Cox, C.T. Gordon, S. Kanae, E. Kowalczyk, D. Lawrence, P. Liu, C.-H. Lu, S. Malyshev, B. McAvaney, K. Mitchell, D. Mocko, T. Oki, K. Oleson, A. Pitman, Y.C. Sud, C.M. Taylor, D. Verseghy, R. Vasic, Y. Xue, T. Yamada, 2004: Regions of strong coupling between soil moisture and precipitation. *Science*, **305**, 1138-1140.

Koster, R.D., Z.-C. Guo, P.A. Dirmeyer, G. Bonan, E. Chan, P. Cox, C.T. Gordon, S. Kanae, E. Kowalczyk, D. Lawrence, P. Liu, C.-H. Lu, S. Malyshev, B. McAvaney, K. Mitchell, D. Mocko, T. Oki, K. Oleson, A. Pitman, Y.C. Sud, C.M. Taylor, D. Verseghy, R. Vasic, Y. Xue, T. Yamada, 2005: GLACE, The Global Land-Atmosphere Coupling Experiment, 1, Overview. Submitted to *J. Hydrometeorology*.

Lawrence, D.M., and J. M. Slingo, 2004: An annual cycle of vegetation in a GCM. Part I: implementation and impact on evaporation. *Clim. Dyn*., **22** (2/3), 87-106.

Lawrence, D.M., and J. M. Slingo, 2004: An annual cycle of vegetation in a GCM. Part II: global impacts on climate and hydrology. *Clim. Dyn*., **22** (2/3), 107-122.

Namias, J., 1960: Factors in the initiation, perpetuation and termination of drought. *Publ. 51*, IASH Commission of Surface Waters, 81-94.

Reale, O., P. A. Dirmeyer, and C. A Schlosser, 2002: Modeling the effect of land-surface variability on precipitation variability. Part II: Spatial and timescale structure. *J. Hydrometeor.*, **3**, 451-466.

Schlosser, C.A., and P.C.D. Milly, 2002: A model-based investigation of soil moisture predictability and associated climate predictability. *J. Hydrometeor*., **3**, 483-501.

Model	SW? Precip.	Rank	SW? ET	Rank	(ET? Precip.)$_1$	Rank	(ET? Precip.)$_2$	Rank
GFDL	0.040	1	0.166	1	0.197	7	0.233	4
NSIPP	0.034	2	0.066	4	0.455	2	0.515	2
CAM3	0.032	3	0.052	8	0.685	1	0.593	1
CCCma	0.024	4	0.110	2	0.379	4	0.209	6
CSIRO	0.014	5	0.058	5	0.096	10	0.241	3
UCLA	0.011	6	0.054	7	0.294	6	0.200	7
CCSR	0.009	7	0.050	9	0.407	3	0.173	8
COLA	0.009	8	0.038	11	0.311	5	0.220	5
GEOS	0.006	9	0.088	3	0.143	9	0.068	10
BMRC	0.005	10	0.043	10	0.156	8	0.114	9
HadAM3	0.002	11	0.057	6	-0.038	12	0.034	11
GFS	-0.004	12	0.013	12	0.040	11	-0.286	12

Table 1. Globally-averaged (over non-ice land points) land-atmosphere coupling strength for all twelve models and in each segment of the path from soil wetness to precipitation, namely soil wetness - ET and ET – Precipitation. (See text for details.)

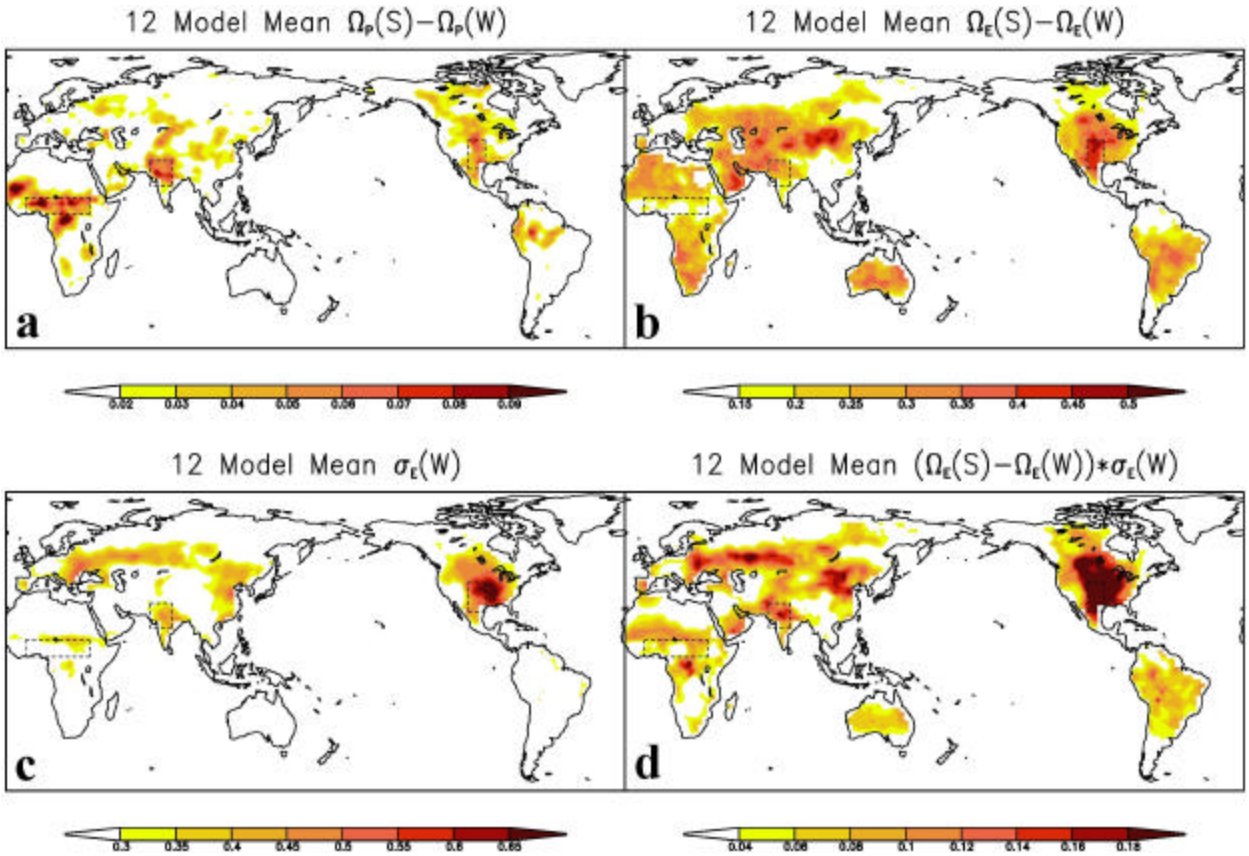

Fig 1. Average of $\Omega_P(S)$- $\Omega_P(W)$, $\Omega_E(S)$- $\Omega_E(W)$, standard deviation of ET, and the weighted coherence diagnostic $(\Omega_E(S)- \Omega_E(W)) \cdot \sigma_E(W)$ across all twelve models.

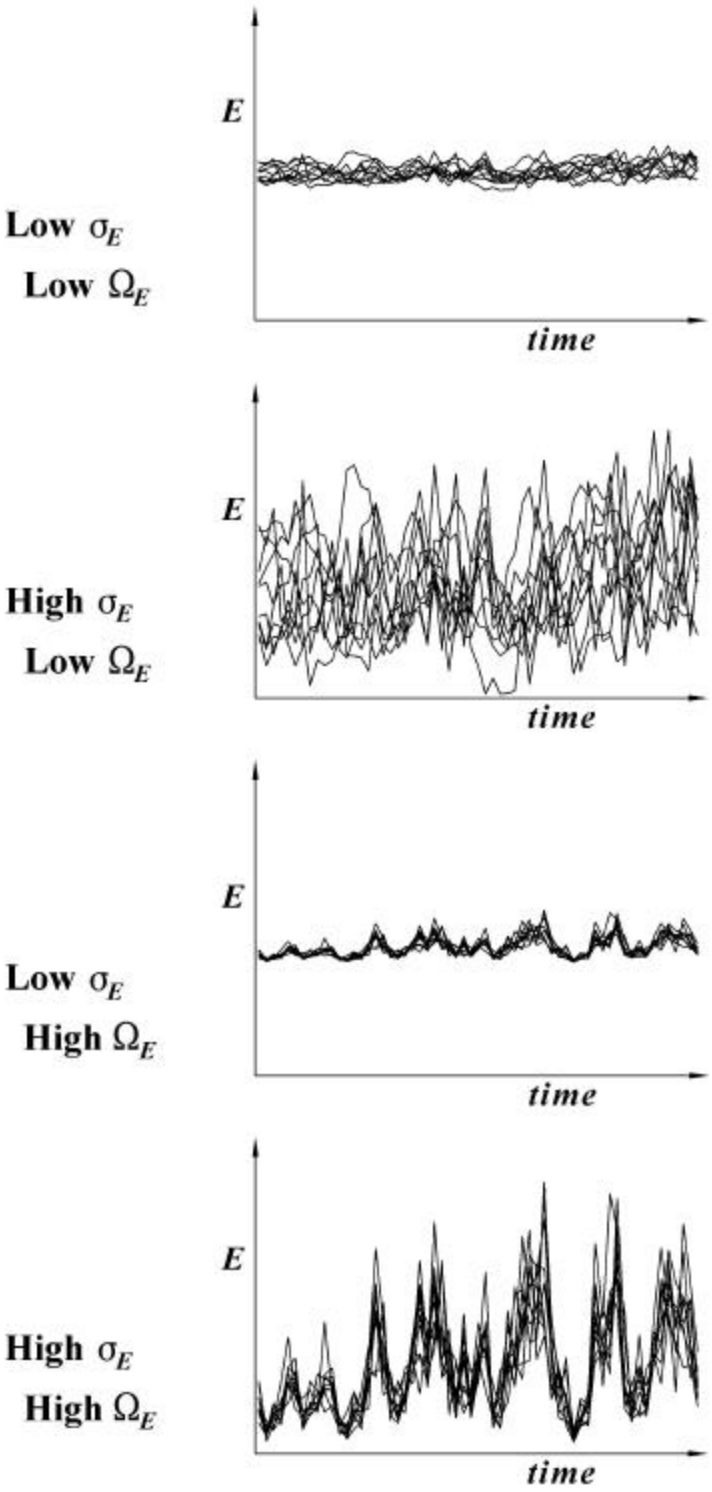

Fig 2. Time series of evaporation for different ensemble members under four situations: (i) low Ω_E with low σ_E, (ii) low Ω_E with high σ_E, (iii) high Ω_E with low σ_E, (iv) high Ω_E with high σ_E. (see text for detail).

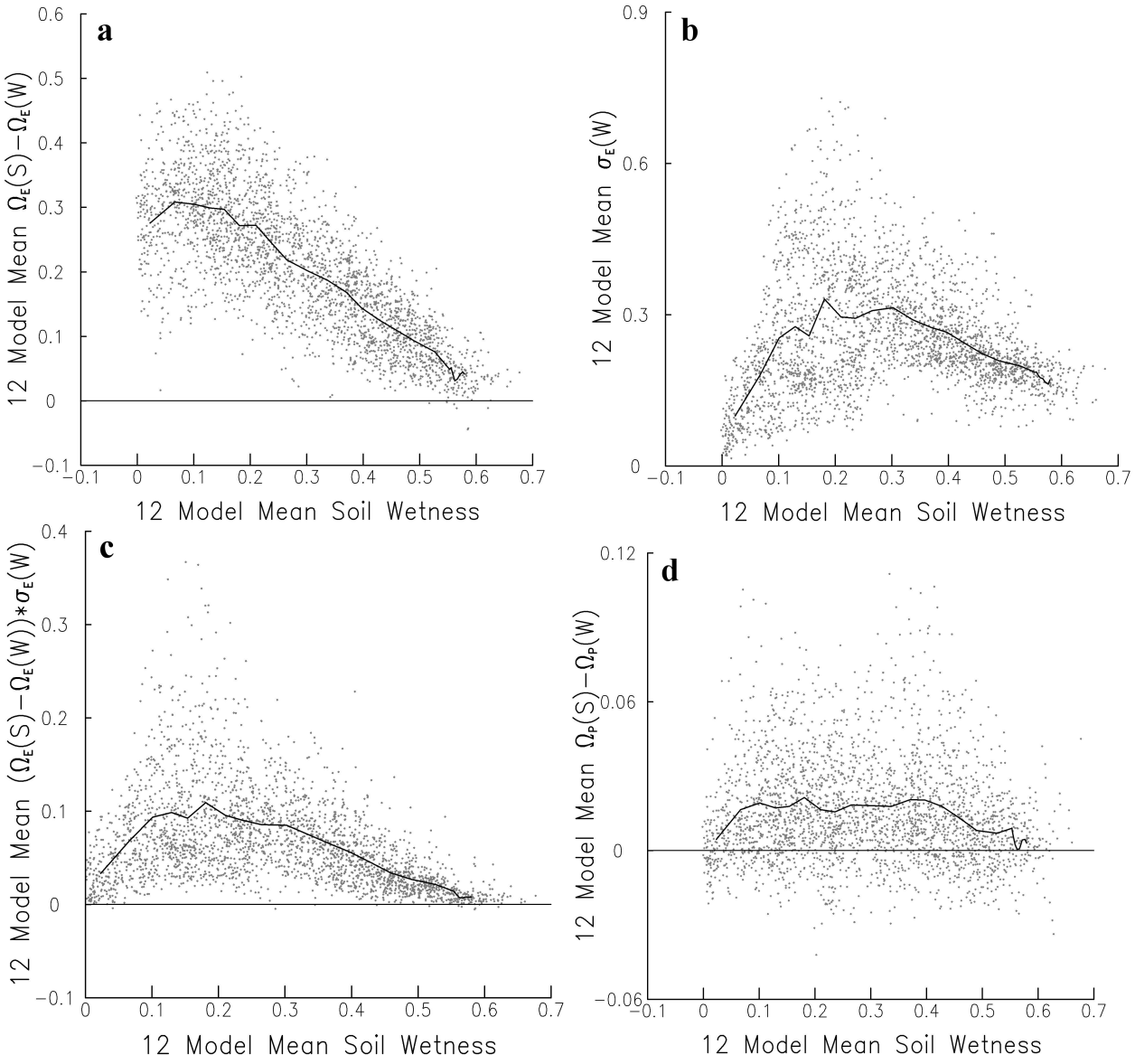

Fig 3. Scatter plots of $\Omega_E(S)-\Omega_E(W)$, σ_E, and $(\Omega_E(S)-\Omega_E(W)) \cdot \sigma_E$ against mean soil wetness. All variables are averaged across the twelve models.

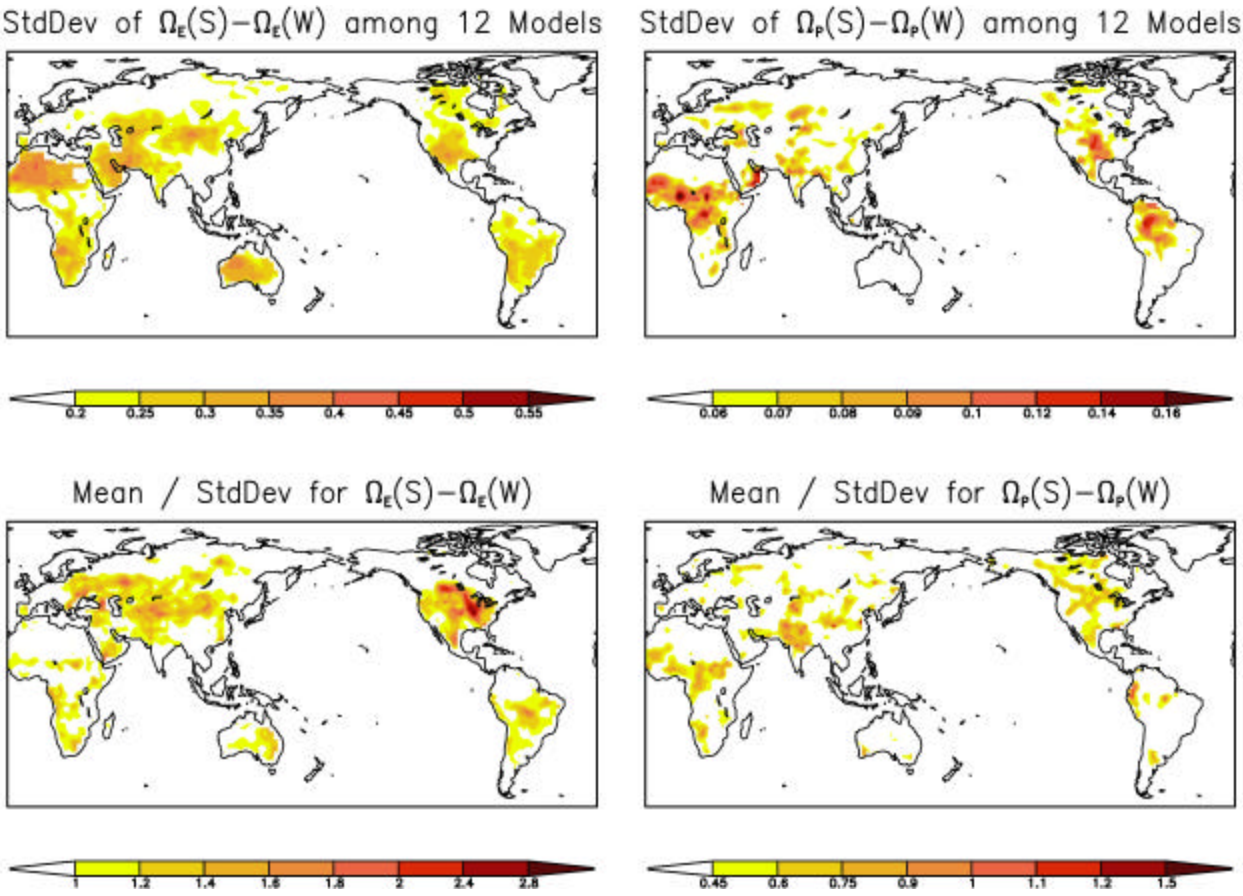

Fig 4. Inter-model standard deviation of $\Omega_E(S)$- Ω_E (W) and $\Omega_P(S)$- $\Omega_P(W)$ among the twelve models (top) and the ratio of the mean to the standard deviation (bottom).

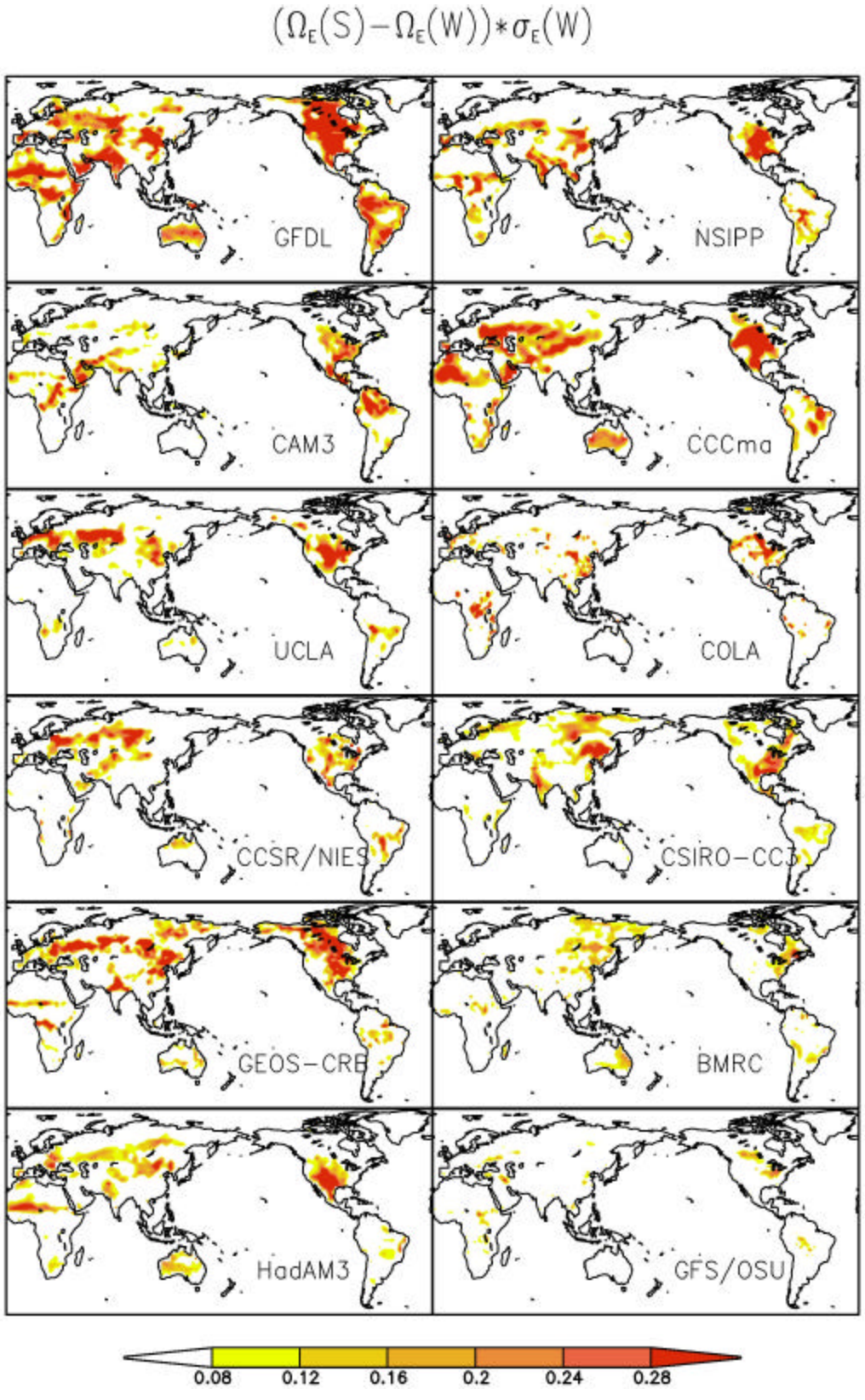

1

2 Fig. 5: Global distribution of $(\Omega_E(S)-\Omega_E(W)) \cdot \sigma_E$ for the models participating in GLACE.

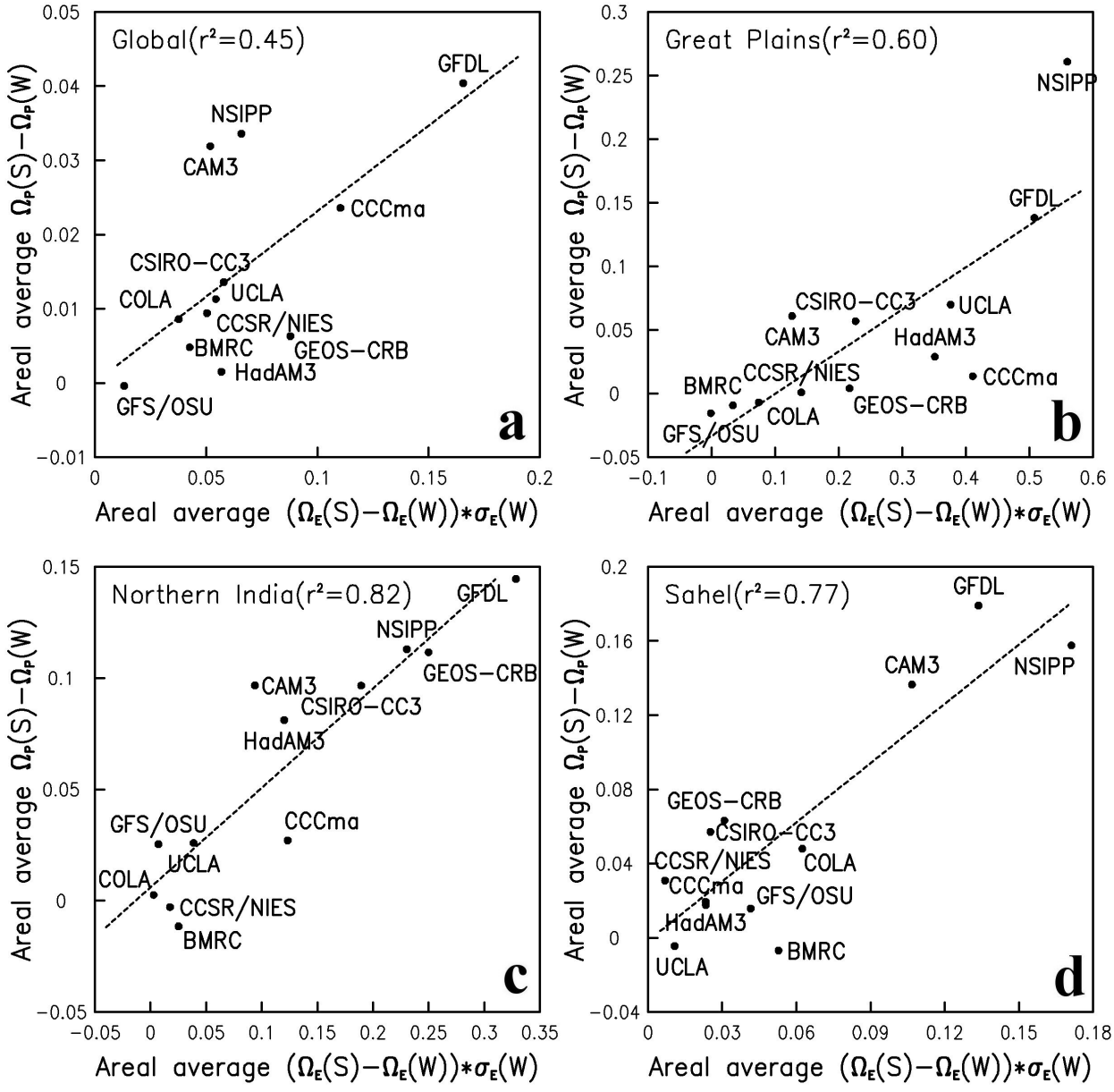

1

2

3 Fig. 6 Areal average of $(\Omega_E(S)- \Omega_E(W)) \cdot \sigma_E$ vs. $\Omega_P(S)- \Omega_P(W)$ over global ice-free land points
4 and some "hot spot" regions (indicated by dashed lines in Fig. 1) for all twelve models.

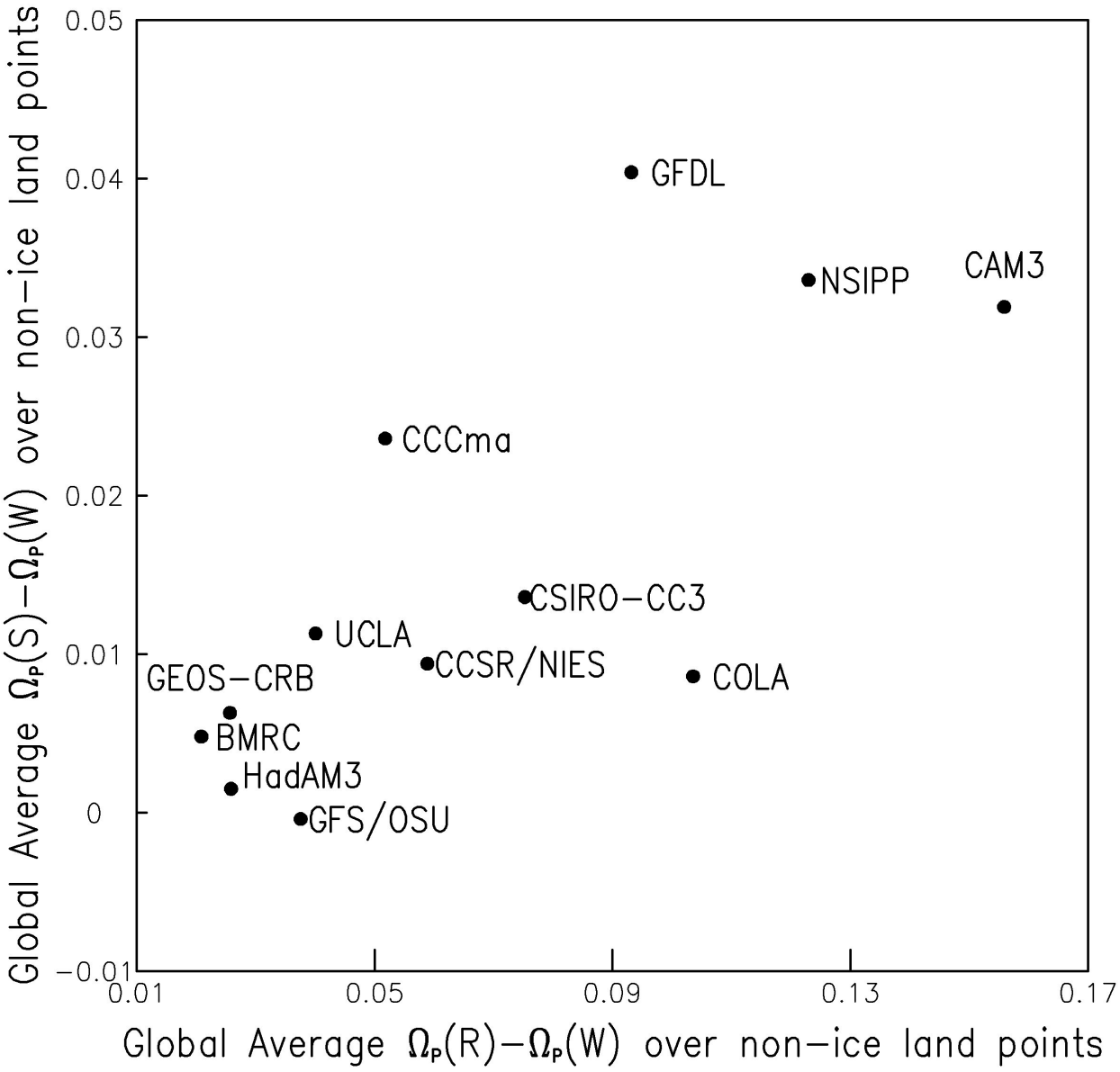

Fig. 7 Global average of $\Omega_P(S)$- $\Omega_P(W)$ vs. $\Omega_P(R)$- $\Omega_P(W)$ over ice-free land points for all twelve models.

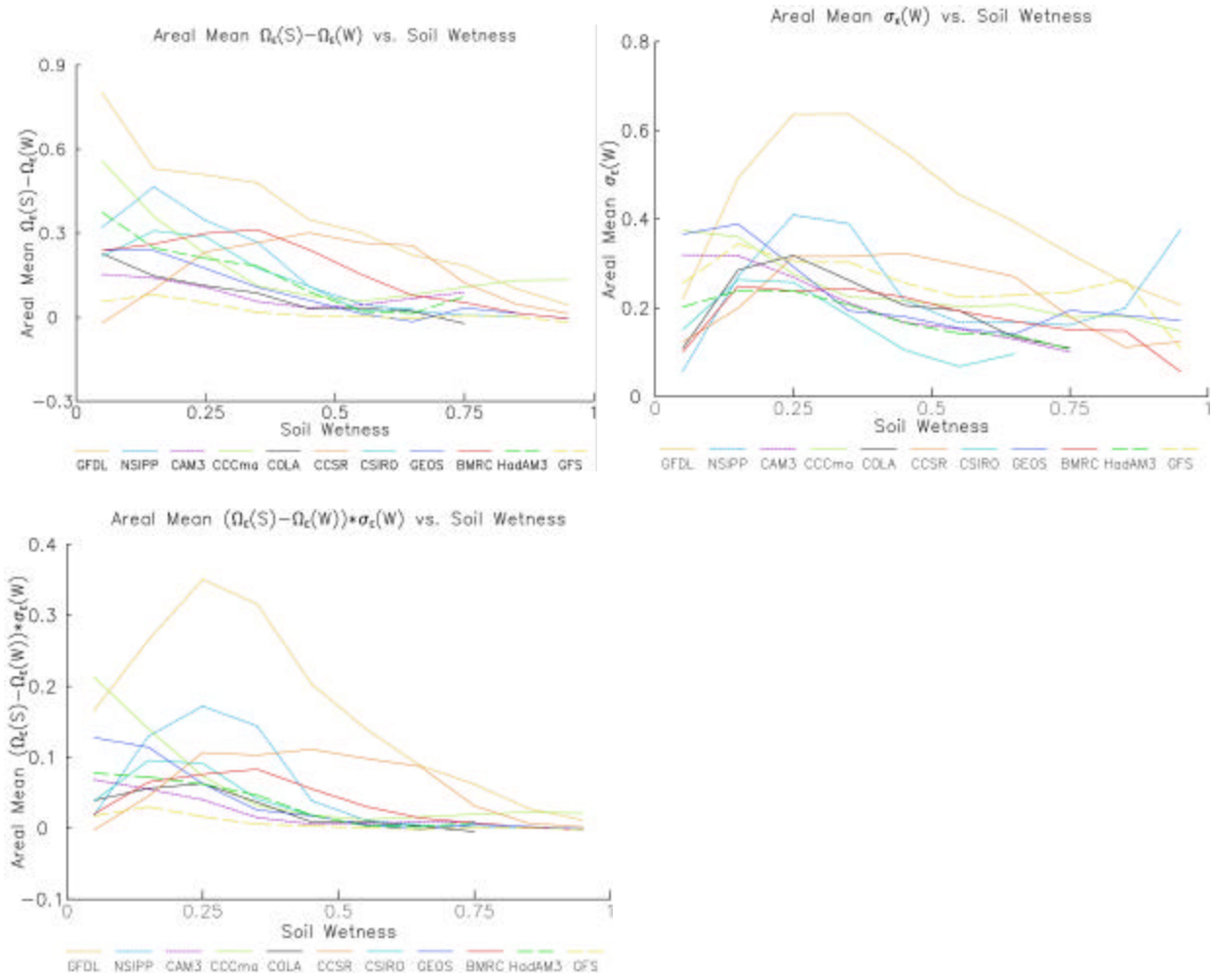

Fig. 8 Areal mean of $\Omega_E(S)-\Omega_E(W)$, σ_E, and $(\Omega_E(S)-\Omega_E(W)) \cdot \sigma_E$ for different climate regimes. (The values for UCLA are not shown because soil moisture values for this model were not available.)

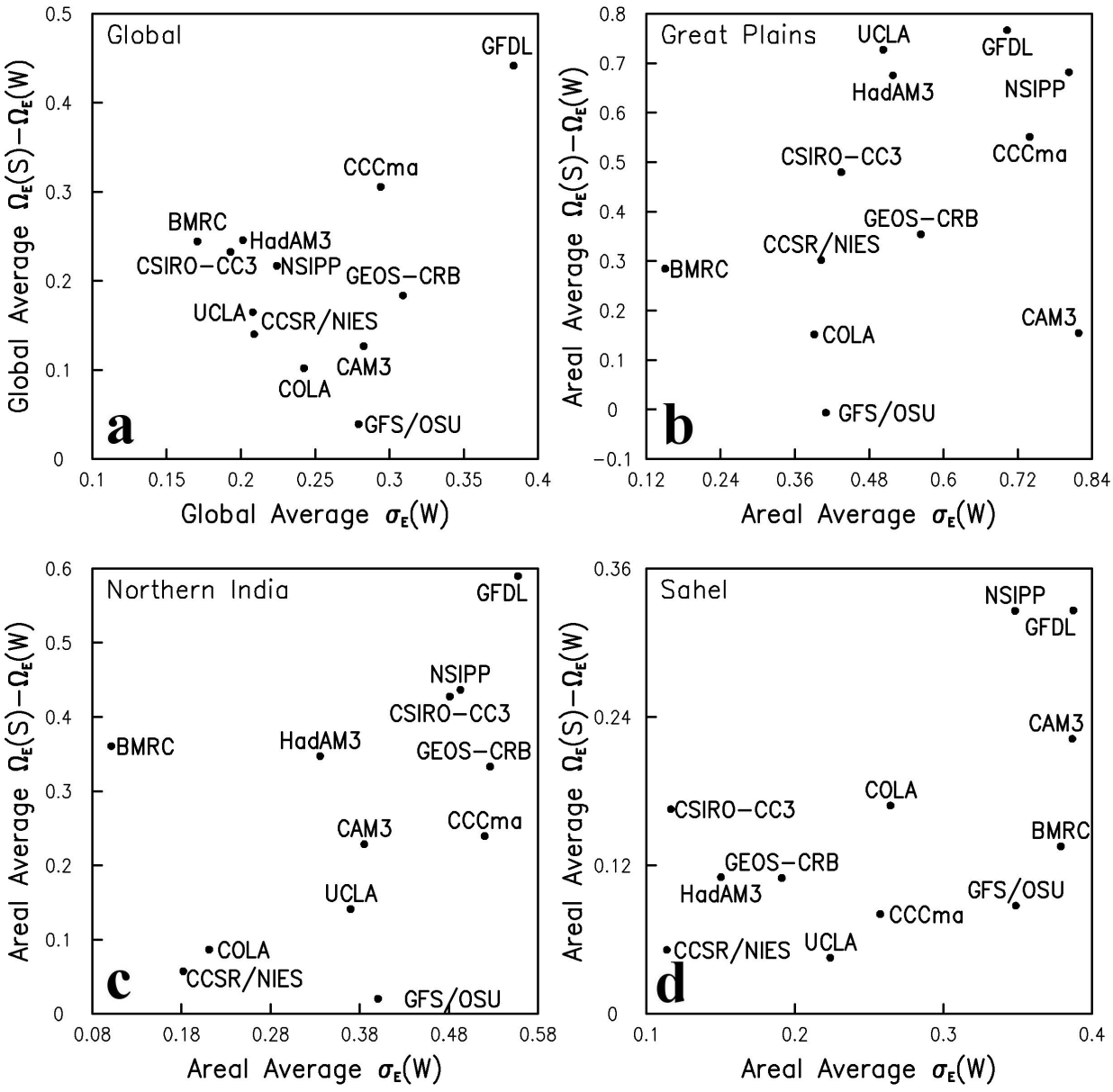

Fig. 9 Areal average of $\Omega_E(S)$- Ω_E (W) vs. σ_E over global ice-free land points and some "hot spot" regions (indicated by dashed lines in Fig. 1) for all twelve models.

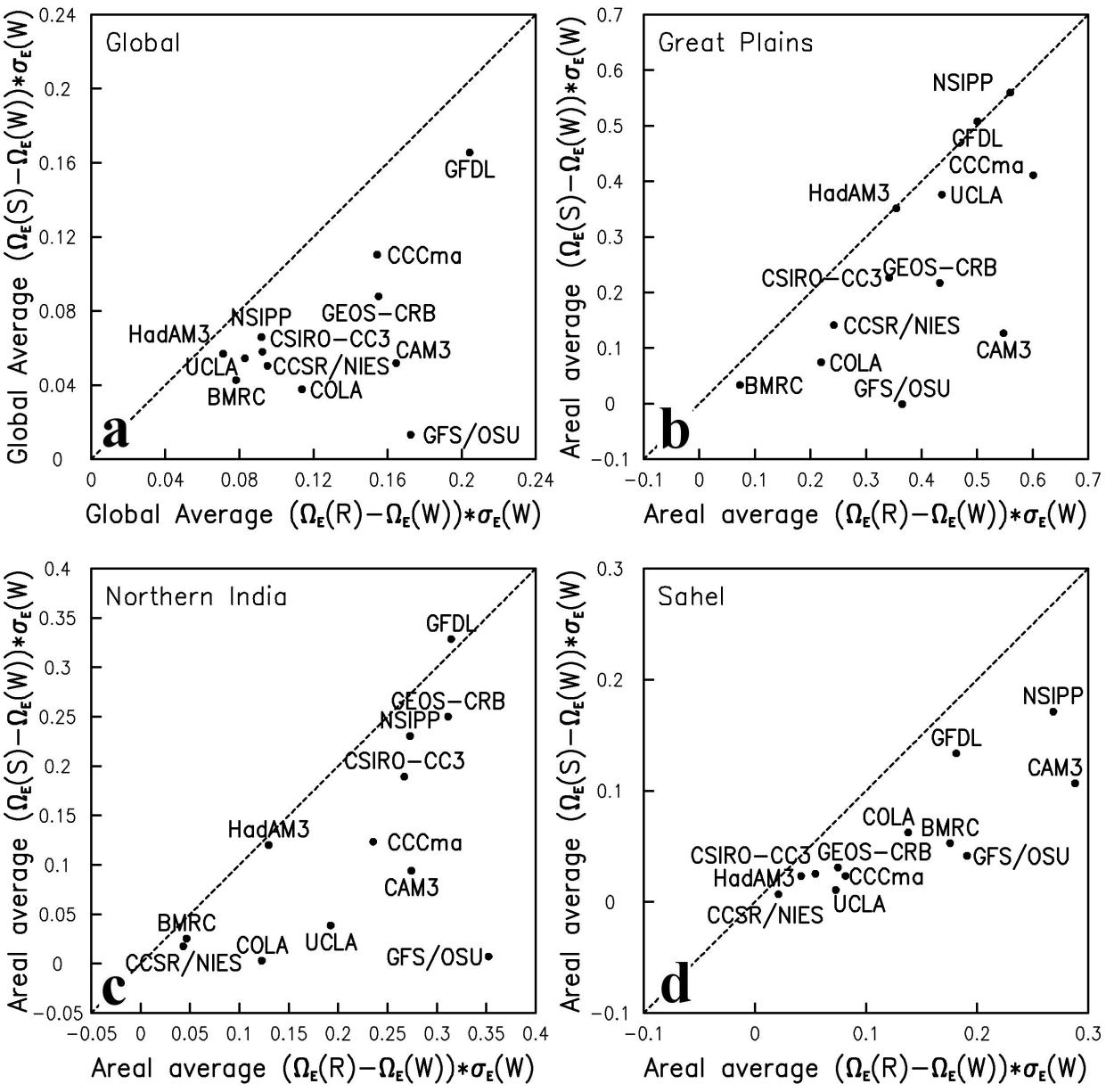

Fig. 10 a. $(\Omega_E(S)- \Omega_E(W)) \cdot \sigma_E$ vs. $(\Omega_E(R)- \Omega_E(W)) \cdot \sigma_E$ for all twelve models, averaged over (a) global ice-free land points, (b) the Great Plains, (c) northern India, and (d) the Sahel. The boundaries of the final three regions are demarcated in Figure 1.

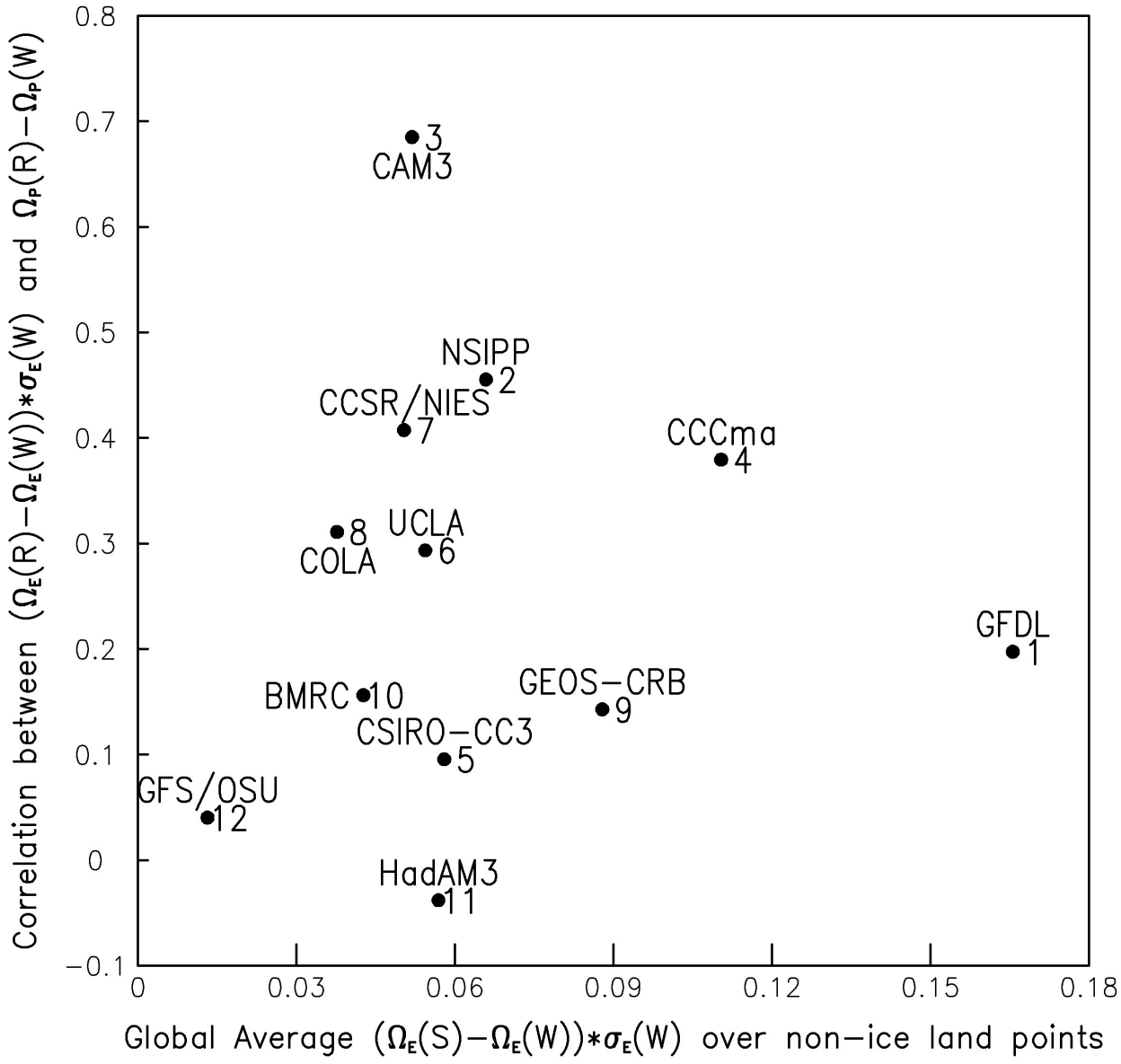

Fig. 11 Global average of $(\Omega_E(S)- \Omega_E(W)) \cdot \sigma_E$ over ice-free land points (a measure of the strength of the soil moisture-evaporation connection) versus spatial pattern correlation between $(\Omega_E(R)- \Omega_E(W)) \cdot \sigma_E$ and $\Omega_P(R)- \Omega_P(W)$ (a measure of the strength of the evaporation-precipitation connection) for all twelve models.

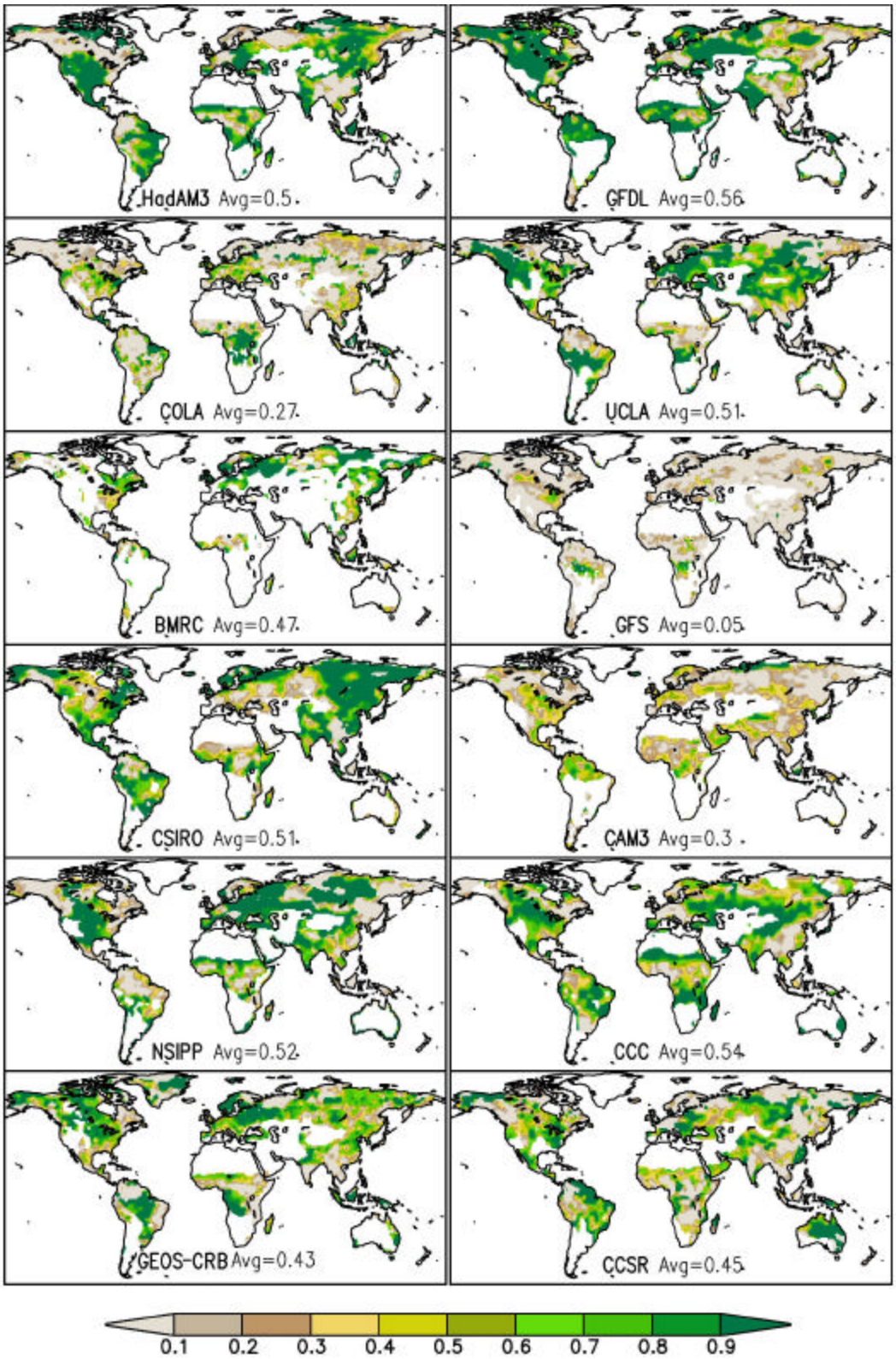

Fig. 12 Global distribution of $[\Omega_E(S)-\Omega_E(W)]/[\Omega_E(R)-\Omega_E(W)]$ for the models participating in GLACE.

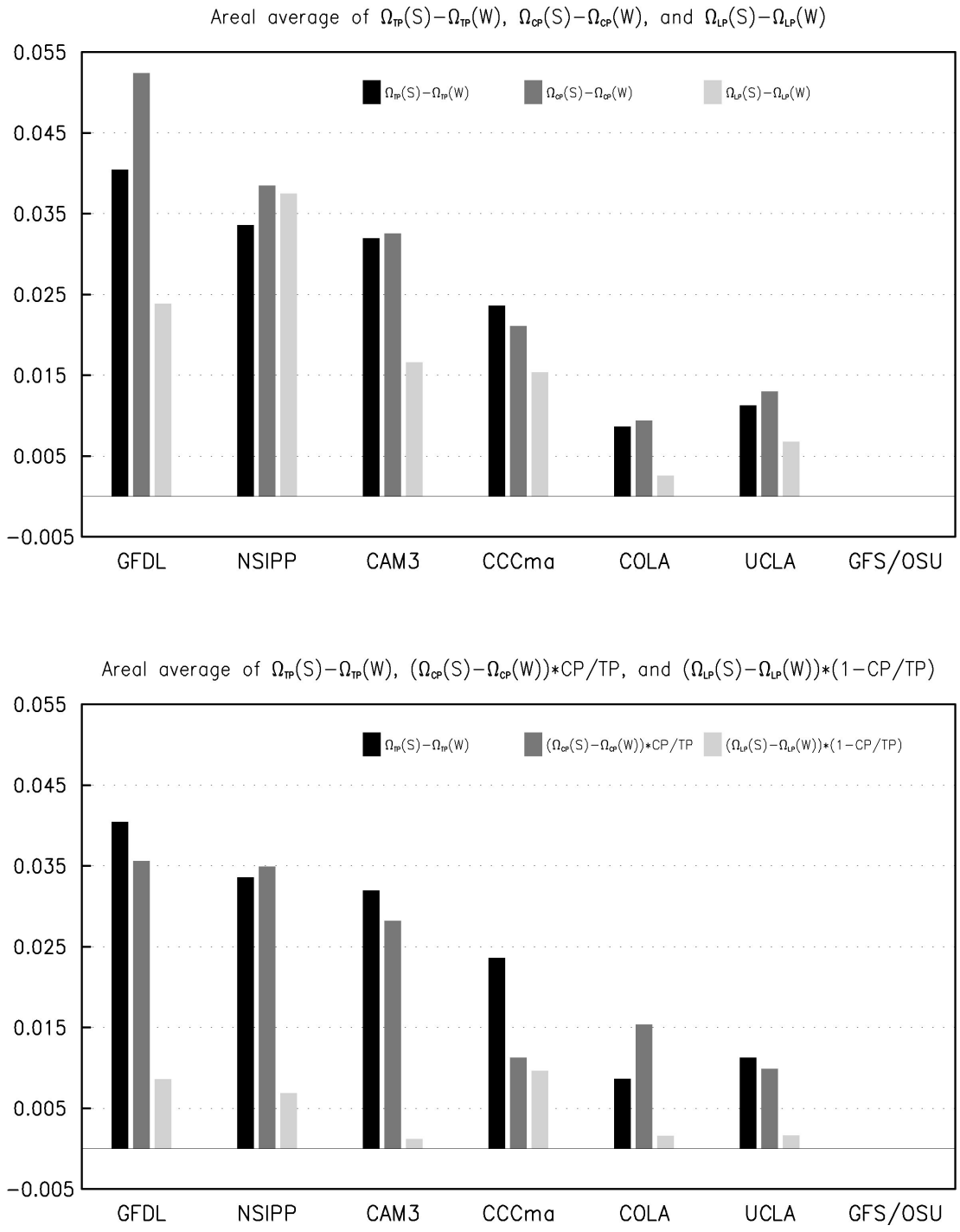

Fig. 13 Global average over ice-free land points of $\Omega_P(S)$- $\Omega_P(W)$ calculated separately from total precipitation, convective and large-scale precipitation components for the models that reported them separately.